Additive Manufacturing 51 (2022) 102604

Contents lists available at ScienceDirect

Additive Manufacturing

journal homepage: www.elsevier.com/locate/addma

Direct evidence of interfacial crystallization preventing weld formation during fused filament fabrication of poly(ether ether ketone)

David W. Collinson [a,1], Natalia von Windheim [b,2], Ken Gall [b], L. Catherine Brinson [b,*]

[a] Department of Mechanical Engineering, Northwestern University, Evanston, IL 60208, USA
[b] Department of Mechanical Engineering and Materials Science, Duke University, Durham, NC 27708, USA

ARTICLE INFO

Keywords:
Atomic force microscopy
PEEK
Additive manufacturing
Fused filament fabrication
Weld formation
Mechanical properties
Strength

ABSTRACT

Poly(ether ether ketone) (PEEK) is a high-performance, semicrystalline thermoplastic that has attracted significant interest for material extrusion additive manufacturing techniques such as fused filament fabrication (FFF) but remains beset by poor weld strength. Here, it is observed that under typical processing conditions that surface crystallization prevents effective weld formation between printed layers, leading to weak and brittle welds. Utilizing atomic force microscopy, differential scanning calorimetry, bulk tensile fracture testing, and mode III tear testing, appropriate processing conditions and post-print annealing conditions have been developed to improve the weld strength of FFF-PEEK. After printing PEEK in an amorphous state through careful control of the thermal gradients during printing a two-step annealing procedure yields crystalline PEEK welds that are 6–8 times stronger than welds in FFF-PEEK that crystallized during printing.

1. Introduction

Poly(aryl-ether-ketones) are high performance polymers that have seen wide interest in high performance applications across numerous industries including aerospace and biomedical applications. In this family of polymers, poly(ether-ether-ketone) (PEEK) is prevalent due to its chemical inertness, excellent mechanical properties and thermal stability when semi-crystalline, making it suitable for a wide range of operating conditions. [1].

There has been significant recent interest in additive manufacturing of custom biomedical implants and other functional parts using PEEK, in particular with material extrusion approaches such as fused filament fabrication (FFF) and powder bed fusion. [2] While fully amorphous polymers are more easily processed by FFF, the thermomechanical performance and high tensile strength offered by PEEK when fully crystallized makes it an attractive material for use in high performance FFF components. [2–4] However, recent efforts with FFF in printing PEEK have been thwarted by poor weld strength between extruded layers that result in highly anisotropic behavior and poor overall part performance. [5–7] Methods developed in response to improve the adhesion between extruded layers have so far had varied success, [8] with annealing procedures and surface treatments generally not improving the strength of FFF-PEEK parts. [9–11] Studies that have utilized hot printing chambers, [12] where hotter chamber temperatures including in excess of 200 °C have showed improvement in mechanical strength and part uniformity, but the influence of chamber temperature on weld strength remains unclear. [11,13–15] By utilizing a slowly crystallizing PEEK compound, a recent study found that prevention of crystallization during printing followed by a subsequent annealing procedure can improve interfacial strength and toughness of FFF-PEEK. [16] Many of the previous studies on FFF of PEEK utilize bulky specimens with extremely complex thermal histories and geometries that convolute the relationship between processing history and weld strength. To enable a direct probe of weld strength, recent efforts utilizing the trouser tear test [17,18] of thin-walled specimens and three-point bending [19] can offer a more direct characterization of weld strength and a targeted analysis on the link between processing history and weld strength. To produce functional FFF-PEEK, devices, a better understanding of the link between processing history of PEEK and its impact on weld strength is desirable.

Investigations on the autohesion of PEEK [20] and other semi-crystalline polymers [21–23] outside of additive manufacturing

* Corresponding author.
E-mail addresses: davidcollinson2020@u.northwestern.edu (D.W. Collinson), natalia.von.windheim@duke.edu (N. von Windheim), kag70@duke.edu (K. Gall), cate.brinson@duke.edu (L.C. Brinson).
[1] Currently at Department of Materials Science, Stanford University, Stanford, California, 94305, USA.
[2] Currently at Center for Design and Manufacturing Excellence, The Ohio State University, Columbus, Ohio, 43212, USA.

https://doi.org/10.1016/j.addma.2022.102604
Received 28 June 2021; Received in revised form 4 January 2022; Accepted 5 January 2022
Available online 10 January 2022

methods has demonstrated that crystallization inhibits the welding of PEEK and other semi-crystalline polymer surfaces above T_g, preventing the formation of strong welds. [24,25] Previous work on PLA [26] has suggested that interfacial crystallization can occur during FFF, limiting part strength due to poor autohesion between the printed layers. Understanding the competing kinetics of weld formation and crystallization in FFF-PEEK is made much more difficult by the complex crystallization behavior of PEEK, [27] the highly non-isothermal nature of FFF [28,29] and the effect of flow induced crystallization on PEEK crystallization kinetics. [30–32]. Whether surface crystallization is responsible for the poor weld formation is FFF-PEEK is still to be established. Identification of surface crystallization as the cause of poor weld strength in FFF-PEEK would enable strategies to improve the weld formation between extruded layers through modification to processing strategies or the formulation of the stock PEEK filament.

This study uses a complementary approach of directly imaging the PEEK microstructure at the welds between extruded layers with atomic force microscopy (AFM) in conjunction with characterization of the weld strength in tension, Mode III crack opening (tear testing) and evaluation of bulk crystallization kinetics. Previous work on acrylonitrile butadiene styrene has shown that the weld microstructure as imaged by AFM can be correlated to the weld strength. [33] The combination of macroscale and nanoscale characterization methods aims to establish how the kinetics of PEEK crystallization and weld formation interact, and whether the weld strength of FFF-PEEK can be improved by carefully controlling the thermal history of the printed part.

2. Methods and materials

2.1. Fused filament fabrication of PEEK

PEEK (Solvay, USA) cylinders, 35 mm tall and 40 mm in diameter with a single layer wall thickness were sliced using Simplify 3D (Fig. 1 (a)) and printed using Aon M2 Industrial 3D printer. Ketaspire™ PEEK filament was placed in a drying oven for at least 4 hrs at 150 °C before printing to remove moisture. Cylinders were printed at multiple chamber temperatures (T_{ch}) of 70 °C, 100 °C and 130 °C (Fig. 1(b-d)) to vary the bulk crystallinity of the print. The 70 °C and 130 °C temperatures represent the upper and lower limits of the system chamber capabilities and 100 °C is the intermediate value between the two limits. While 130 °C is only a moderate chamber temperature, with some systems utilizing 200 °C or higher chamber temperatures, [12] it was sufficient for the PEEK to reach a high crystalline fraction of ~32%. All other print parameters were kept constant and are given in Table 1.

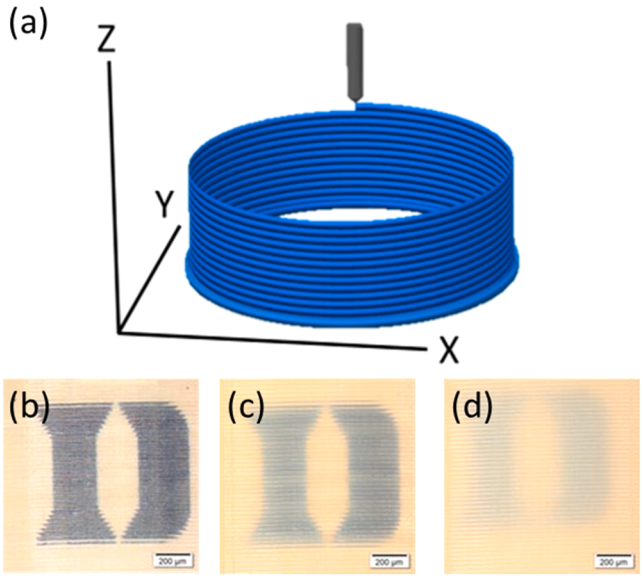

Fig. 1. (a) Schematic of Simplify3D "vase mode" continuous spiral toolpath to create a FFF-PEEK single-walled cylinder. Optical images displaying opacity of as-printed cylinders with (b) 70 °C, (c) 100 °C, and (d) 130 °C build chamber temperatures. Scale bars are 200 μm.

For AFM samples, the weld interfaces of cylinders printed with the 100 °C and 130 °C chamber temperatures were too weak to survive AFM sample preparation. Instead, samples prepared for AFM were printed as thin-walled rectangular prisms with a 20 mm side length and 70 mm height, a layer height of 125 μm, and T_{ch} = 70 °C. These conditions yielded visually crystalline samples with an average crystalline fraction of 9% as measured by DSC, comparable to the cylinders printed for mechanical testing with T_{ch} = 100 °C.

2.2. Annealing of printed PEEK specimens

All post-print heat treatments were conducted with a vacuum oven (Sheldon Manufacturing, USA). To examine the impact of iso-thermal annealing, samples printed with T_{ch} = 70 °C were annealed for a total of 12 hrs at 148 °C or 180 °C. These two temperatures were chosen after analysis of the PEEK crystallization kinetics (Section 3.4). In addition, a multiple step anneal was conducted where samples were first annealed at 148 °C for 6 hrs to promote weld healing and then ramped for a second anneal at 180 °C for another 6 hrs for crystallization. Heating and cooling ramp rates were conducted at 1 °C/min unless otherwise stated. Due to the high sensitivity of the PEEK crystallization kinetics to temperature near 148 °C, the oven was initially ramped to 135 °C and held until the oven temperature stabilized. Then the temperature was ramped to 148 °C at 0.5 °C/min to prevent overshoot and undesired crystallization.

2.3. Differential scanning calorimetry

The crystallinity of the printed cylinders was determined using DSC (Discovery 2500, TA Instruments, United States). Unless otherwise specified, approximately 10 mg was extracted for each sample from the thin-walled cylinder samples. For each print and anneal condition, 3 samples were taken at evenly spaced positions along the z axis of the cylinder, while avoiding the bottom 5 mm due to the proximity of the heated build plate affecting the local thermal history. Samples were heated at 10 °C/min in a nitrogen environment to measure the enthalpy. The percent crystallinity was determined from the first pass ΔH_m divided by the theoretical ΔH_m of 130 J/g for 100% crystalline PEEK. [34] Calibration was performed with an Indium standard.

2.4. Tear testing

Weld tear strength measurements were conducted according to the protocol outlined in Seppala *et. al.* [18] Samples 5 mm wide and 60 mm long were cut as shown in Fig. 2(a)) so that crack propagation would occur along a weld between extruded layers. To account for any intra-sample variability in thermal history, tear specimens were taken from a variety of locations within each cylinder. However, the proximity of the heated base plate near the bottom of the cylinder led to observable local changes in the crystallinity of the extruded layers and so the bottom 5 mm of the printed cylinders was avoided during preparation of

Table 1
Fixed print parameters for the fused filament fabrication of PEEK cylinders used for testing.

Parameter	Value
Nozzle Temperature	395 °C
Nozzle Diameter	0.25 mm
Print Speed	1500 mm/min
Layer Height	0.175 mm

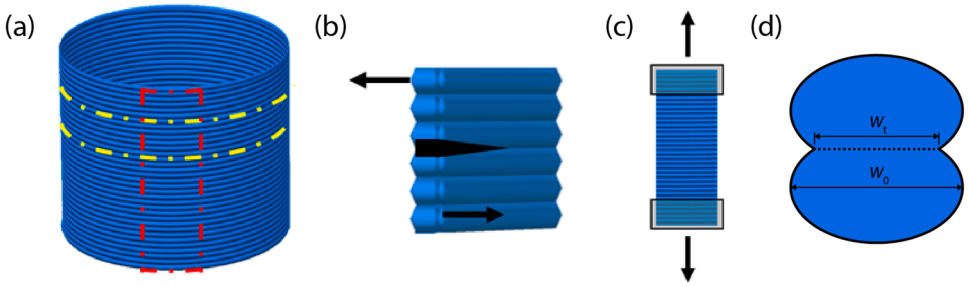

Fig. 2. (a) Schematic of sample cuts for tear testing (yellow) along the weld lines and tensile testing (red) perpendicular to the weld. (b) Tear testing setup with a pre-crack along a weld line and the two free ends pulled apart to drive Mode III crack propagation. (c) Tensile testing setup with grayed regions representing the epoxy reinforced grip section. (d) Schematic of sample cross-section showing the measured location of the wall thickness, w_0 and the weld thickness, w_t.

tearing specimens. A sharp razor was used to form a precrack along the weld in the center of each tearing specimen.

The nominal tearing energy for amorphous and crystalline PEEK was determined from trouser tear tests of 30 μm thick, amorphous, PEEK (Ketaspire™, Solvay, USA) films before and after cold crystallization at 180 °C for 12 hrs. Film samples were cut to standard ASTM D1938 [35] dimensions and the precrack was initiated with a sharp razor blade.

An RSA G2 DMA (TA Instruments, USA) was used to conduct the trouser tear test. Each leg of the sample was clamped and pulled at a constant rate of 50 mm/min (Fig. 2(b)) until the weld had completely torn. The tearing strength of the weld, T can then be calculated from the average force during stable tearing, F and the width of the weld, w_t using Eq. 1.

$$T = \frac{2F}{w} \tag{1}$$

Due to necking at the weld interface, the actual weld thickness, w_t is smaller than the overall wall thickness, w_0. (Fig. 2(d)). Optical microscopy was used to measure the w_t and w_0 for all printing and annealing conditionsand are provided in Table 2. The weld thickness w_t was used in Eq. 1 to calculate T instead of w_0 for better comparison to the film samples used to measure the bulk tearing energy of PEEK.

2.5. Tensile testing

The tensile strength of the printed cylinders was determined through monotonic tensile testing (Test Resources 830EL63) of strip samples cut out of the cylinders. A razor blade cut perpendicular to the weld was used to create the strip subsections (Fig. 2(a)). The strips were 10 mm wide and between 10 and 35 mm long (total height of cylinder), depending on if cracks formed along the welds during cutting. The part of the sample placed in the tensile grips was reinforced with epoxy (J-B Weld) (Fig. 2(c)). Tensile strips were tested at a displacement rate of 1 mm/min until failure. Failure is defined as the fracture of the printed welds in the sample resulting in a decrease in stress. The cross-section dimensions of samples were measured with calipers before testing. Strain was measured by marking tracking points on the sample before testing and using a video extensometer system.

Table 2
Wall thickness and weld width dimensions in the as-printed samples at three chamber temperatures and after post annealing of samples printed with T_{ch} = 70 °C. Error values reflect the standard distribution across a sample of 10 welds.

Process Temperature (°C)	Wall Thickness, w_0 (μm)	Weld Thickness, w_t (μm)	w_t/w_0
$T_{ch} = 70$	356 ± 17	263 ± 13	0.74 ± 0.05
$T_{ch} = 100$	355 ± 11	277 ± 5	0.78 ± 0.03
$T_{ch} = 130$	338 ± 9	258 ± 8	0.76 ± 0.03
$T_A = 148$	370 ± 9	268 ± 7	0.72 ± 0.03
$T_A = 180$	352 ± 13	267 ± 8	0.76 ± 0.04
$T_A = 148$ and 180	371 ± 12	275 ± 10	0.74 ± 0.03

2.6. Atomic force microscopy (AFM)

Atomic force microscopy (AFM) scans were collected across the weld region between extruded layers of select samples to observe polymer structure and crystallinity at the interface between extruded layers. First, sections were cut from sample printed for AFM analysis using a diamond saw to minimize plastic deformation to expose the cross-section of the extruded layers as well as the weld interfaces. The exposed surface was wet sectioned at room temperature with a UC7 Ultramicrotome (Leica, Germany) to produce a smooth surface, with an R_a = 0.56 nm as measured by AFM in the amorphous regions of the samples. The cutting direction during sectioning was perpendicular to the weld interface to preserve the weld structure.

A Cypher ES (Asylum Research, USA) atomic force microscope (AFM) was used in tapping mode to collect images weld region (Fig. 2 (d), to observe the change in morphology of crystalline domains, if any, at the weld interface. Measurements were acquired with a AC240 probe (Olympus, Japan) using the 1st or 3rd eigenmode of the cantilever. The 3rd eigenmode is used as the high effective stiffness and resonant frequency enables stable and fast scanning over the crystalline domains while maintaining low forces due to the small oscillation amplitudes used. The measurement parameters used for image acquisition are provided in the caption of the relevant data set.

For mechanical property measurement, AM-FM (amplitude modulated – frequency modulated) AFM was performed with the cantilever of an AC240 probe excited at its 1st and 2nd eigenmodes simultaneously. [36] The observable phase shift of the first eigenmode, ϕ_1 and frequency shift of the 2nd eigenmode, Δf_2 during scanning can be converted into an elastic modulus, E_{punch} and loss tangent (tan ϕ) according to Eqs. 3 and 4. [37–39].

$$E_{punch} = \frac{\pi}{\sqrt{6R}}\left(2k_2\frac{\Delta f_2}{f_2}\right)^{1.5}\left(\frac{k_1}{Q_1}\frac{A_{0,1}}{A_1}\cos\phi_1\right)^{-0.5} \tag{2}$$

$$\tan\varphi = \frac{A_1/A_{0,1} - \sin\phi_1}{\cos\phi_1} \tag{3}$$

where R is the punch radius of the tip, k_1 and k_2 are the 1st and 2nd eigenmode stiffnesses respectively, f_2 is the 2nd eigenmode resonant frequency, Q_1 is the 1st eigenmode quality factor, $A_{0,1}$ and A_1 are the free-air amplitude and amplitude setpoint of the 1st eigenmode respectively and $\phi_1$is the phase shift of the 1st eigenmode. All final tuning of the cantilever was conducted 500 nm above the sample surface. The surface deformation due to indentation, δ_{max} as calculated by Eq. 5, [40] was used to correct the height maps as follows in Eq. 6.

$$\delta_{max} = \frac{A_1 k_1}{2Q_1 k_2}\frac{\cos\phi_1}{\Delta f_2/f_2} \tag{4}$$

$$h_{true}(x,y) = h_{obs}(x,y) + \delta_{\max}(x,y) \quad (5)$$

3. Results and discussion

The following results first examine the bulk crystallinity and mechanical strength of the as printed welds printed at three different chamber temperatures in tension and Mode III crack opening conditions. AFM imaging of the distribution of crystallinity in the sectioned layers is then conducted to understand the significant decrease in weld strength with increasing chamber temperature. Finally, annealing procedures are developed to improve the strength of the crystalline PEEK welds post-print.

3.1. Bulk crystallinity and mechanical testing of FFF-PEEK welds

The samples printed at the three chamber temperatures were first analyzed in DSC to establish the bulk crystallinity of the as-printed samples. Examples of the heat flow traces acquired on heating are provided in Fig. 3. A clear transition in cold crystallization behavior can be observed above the T_g of the as-printed PEEK with increasing chamber temperature. The cold crystallization enthalpy peak is strongest for the samples printed at $T_{ch} = 70$ °C, still present for the samples printed at $T_{ch} = 100$ °C, and no cold crystallization is observed for the $T_{ch} = 130$ °C samples.

Measurement of the enthalpy of cold crystallization and the melt enthalpy allows for a calculation of the as-printed crystalline fraction (Table 3). Calculation of the as-printed sample crystallinity shows very little crystallinity for the samples printed at 70 °C and 100 °C whereas the samples printed at 130 °C has completely crystallized. The increase in crystalline fraction for the $T_{ch} = 130$ °C is accompanied by an increase in the measured T_g of the sample. These results are consistent with fundamental understanding that rapid cooling of a polymer sample suppresses crystallization and leads to cold crystallization as the sample is then heated past T_g in a DSC run. Thus, in these data, the lower chamber temperatures allowed limited crystallization during printing, while the highest chamber temperature was close enough to T_g to allow full crystallization to occur in the as-printed sample.

To compare the strength of the crystalline and amorphous welds, Mode III crack opening a are performed according to Section 2.4 for each of the three chamber temperatures tested: 70 °C, 100 °C and 130 °C. Examples of the tearing curves and tensile stress-strain curves acquired for each chamber temperature is provided in Fig. 4(a) and (b) respectively. Stable tearing can be observed on the welds printed with the

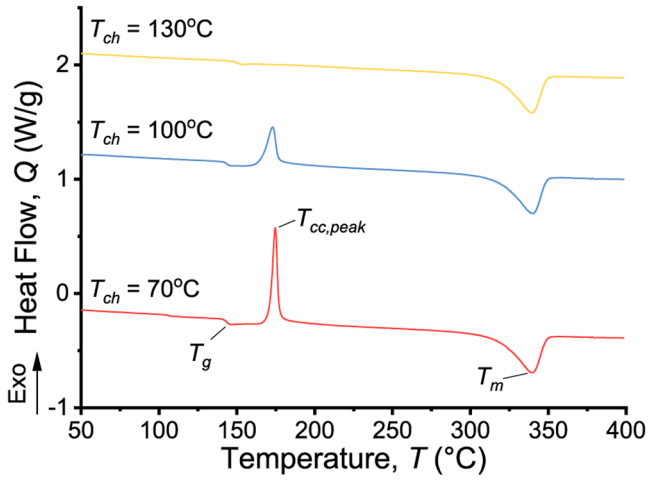

Fig. 3. DSC traces of FFF-PEEK samples printed at three chamber temperatures. Upon increasing the chamber temperature, the as-printed crystallinity increases, reducing the amount of cold crystallization possible during heating in the DSC.

70 °C chamber temperature at a steady-state force of approximately 4 N required to maintain crack growth. For the samples printed at the higher temperatures, crack growth was unstable, with stick-slip tearing indicating brittle fracture along the weld. Isolated periods of stable crack growth can be observed in the 100 °C force-displacement curves, and generally require high forces to initiate unstable crack growth. The resulting nominal tearing strength calculated from averaging the force over the draw distance shows a dramatic decrease in weld strength as the chamber temperature is increased (Fig. 4(c)). The tensile stress-strain curves show that samples printed at $T_{ch} = 70$ °C are the strongest while samples printed at $T_{ch} = 130$ °C are particularly weak in tension. All samples failed at the welds between extruded layers, regardless of chamber temperature. Quantifying the elastic modulus and ductility of the samples in tension is complicated by the non-ideal sample geometry and the apparent interfaces of the printed layers on the measurement of strain with the video extensometer used in this study.

The decrease in weld tearing strength with an increase in chamber temperature from 70 °C to 130 °C is correlated to the decrease in ultimate tensile strength (Fig. 4(c)) suggesting that, for the tested sample geometry, the strength of the weld (as measured by trouser tear experiments, Fig. 2(b)) controls the overall strength of the sample in tension. It should be noted while the trouser tear test samples a single weld to be tested for tearing strength, measurements of UTS in tension (Fig. 2(c)) applies a load across multiple welds, the weakest of which will define the UTS. The degradation of FFF-PEEK tensile strength observed here with as ccrystalline fraction is increased is at odds with the expectation from the literature [4,41] that bulk PEEK tensile strength improves with increased crystalline fraction. . The observed correlation between the decrease in weld strength and UTS within the range of chamber temperatures tested therefore indicates that local changes at the weld between the extruded layersmay be primarily responsible for the poor mechanical properties observed in the highly crystalline samples. To examine whether the mechanism causing poor mechanical strength can be identified, AFM is used to directly examine local weld structure.

3.2. Distribution of crystallinity in the extruded layer

The first step in understanding the weld microstructure was direct imaging of the distribution of crystallinity across an extruded layer within a printed sample. The distribution of spherulites was determined using AFM to map the locations of the spherulites at nanometer scales in the bulk and interfacial regions. The sectioned sample was imaged first with optical microscopy under DIC (differential interference contrast) as shown in Fig. 5(a) to obtain a high-level map of crystallinity followed by targeted AFM for higher resolution and surface detail (Fig. 5(b-c)) across regions of interest.

The optical image under DIC contrast conditions indicates an irregular distribution of crystallinity throughout the printed specimen (Fig. 5 (a)). Here the crystalline domains manifest themselves in the height data channel due to the rough local surface topology compared to the relatively featureless amorphous regions of the polymer.We suggest that during sectioning the crystalline domains fracture along preferential planes depending on the orientation of the crystallite lamellae relative to the cutting direction. As such the individual lamellae with fracture surface normals that are not coincident with the surface normal of the cutting plane cause topological variation in the sectioned sample. In comparison the amorphous regions have no preferential fracture direction and appear relatively smooth. The streaks that can be observed in the AFM images are due to cutting marks from the ultramicrotomy. Porosity can also be observed as bright features in the DIC image at the weld lines between the extruded layers.

AFM imaging of an extruded layer cross-section, Fig. 5(b), shows that a higher density of crystalline domains can be observed in the center of the extruded layer with the density of spherulites gradually decreasing radially until there is minimal crystallinity in the extruded layer within

Table 3
DSC characterization of the as-printed crystallinity for each of the three build chamber temperatures tested. 3 samples were tested for each chamber temperature. Provided values represent the average across all three samples and the error represents the standard deviation.

Build Chamber Temp (°C)	Glass Transition Temperature, T_g (°C)	Cold crystallization onset temperature, $T_{cc,onset}$ (°C)	Cold crystallization peak temperature, $T_{cc,peak}$ (°C)	Melt Temperature, T_m (°C)	Enthalpy, ΔH (J/g)	As-printed crystalline fraction (%)
70	143.2 ± 0.1	171.0 ± 0.2	174.7 ± 0.1	339.6	10.3 ± 2.0	8 ± 2
100	143.0 ± 0.3	165.6 ± 0.3	172.8 ± 0.04	339.7	10.1 ± 3.3	8 ± 3
130	149.2 ± 0.3	–	–	339.5	42.3 ± 0.4	32 ± 2

approximately 15 μm of the weld lines. However, a significant fraction of both welds is occupied by crystalline domains. Additional imaging of one of the weld lines (Fig. 5(c)) confirms that the weld line is almost entirely occupied by crystalline domains. The decrease in PEEK crystallinity outwards from the center of the extruded layer was predicted by Pu *et. al.* [42] and explained to be due to a spatially commensurate increase in the local cooling rate reducing the time for crystal growth before the material decreases below T_g and molecular motion is ceased. However, the high number of crystallites observed along the weld line in this study is in conflict with the suggestion by Pu *et. al.* that the weld interface is amorphous. Therefore, some additional mechanism to explain the high interfacial crystallinity beyond standard quiescent crystallization models is needed. Modelling conducted by McIlroy *et. al.* [43] that includes flow induced crystallization shows a highly crystalline interface, consistent with what is observed in this study. The presence of this interfacial crystallinity could limit the formation of welds between printed extruded layers, degrading bond strength. Identification of the mechanisms causing interfacial crystallization at the weld line will help enable manufacturing procedures to promote strong welds and improve the mechanical strength of FFF-PEEK.

AM-FM mechanical property maps were conductednear the weld interface (Fig. 6) and include both crystalline domains and the adjacent amorphous regions. These regions showed a consistent nodular structure with varying modulus and loss tangent which may be the result of frozen-in, nematic crystals formed during extrusion due to shear induced alignment of PEEKs rigid, rod-like chain backbone. [30–32,44–46] A large-scale height image shows the strongly crystalline weld interface, (Fig. 6(a)) with spherulites and a crystalline region along the weld line observable. Fig. 6(b-c) show the left-hand side and right-hand side respectively of the interface between the crystalline layer and the amorphous portion of the extruded layer with the corresponding maps of modulus and loss tangent shown in Fig. 6(d-e) and Fig. 6(f-g) respectively. The dense number of crystallites at the interface suggests a high number of nucleation sites and rapid growth of crystalline domains compared to the neighboring bulk material, which is predominantly amorphous. While no 'shish-kebab' structures, which are indicative of flow induced crystallization, are observed here; flow induced crystallization can cause increased spherulitic nucleation density [47] and may be responsible for the high number of crystalline domains observed near the interface.

Comparison of the crystalline and amorphous regions in Fig. 6(d-g) suggests there is no significant difference in the elastic modulus and loss tangent of the crystalline domains compared to the neighboring amorphous domains (Fig. S1 in the supporting information). Instead, increased surface roughness is the likely the cause behind of the wider distribution in modulus and loss tangent observed on the crystalline domains. Some systematic difference in the average modulus and loss tangent between Fig. 6(d, e) and Fig. 6(f, g) is also observed and attributed to a small amount of instrumental drift. High resolution images of the elastic modulus (Fig. 6(h)) and loss tangent Fig. 6(i)) on the amorphous region indicated in Fig. 6(d) show that the variation in modulus and loss tangent are positively correlated. In Fig. 6(d-e) nodules with either significantly lower or higher modulus than the surrounding material can be observed and examples of each are indicated with arrows in Fig. 6(h). The anomalous nodules are not correlated with strong contrast in the height maps (Fig. 6(b-c)) and cannot be attributed to surface roughness. Instead, they may be the result of defects in a frozen mesophase. [31].

3.3. Influence of thermal history

Near the heated printer bed, the printed cylinder sample transitions to being highly crystalline as a result of the heated bed slowing the cooling rate of extruded layers after deposition. Further investigation on the crystalline extruded layers near the print bed and the amorphous extruded layers further away indicates that the weld interface is consistently crystalline no matter whether the bulk of the extruded layer is amorphous or crystalline. A bright field optical image of the ultramicrotomed surface in Fig. 7(a) highlights the significant variation in crystallinity observable between extruded layers at the macroscopic scale as a result of the variation in the temperature of the hot end and proximity to the heated build plate. To interpret Fig. 7(a), note that the predominantly amorphous regions of the part are transparent and therefore dark in the optical image, while the spherulites scatter the incident light, making crystalline regions opaque.

Thus, the optical image in Fig. 7(a) illustrates a transition across the printed part such that the base of the sample near the heated plate is predominantly crystalline while regions further removed transition to being predominantly amorphous. The change in degree of crystallinity is expected to be related to the local thermal history, with layer-by-layer variation of crystallinity likely due to instability in the temperature of the nozzle. From this cross-section, locations that are representative of each of the amorphous, partially crystalline, and crystalline regions are identified and marked with (b), (c) and (d) in Fig. 7(a).

AFM height images on each of the regions indicated in Fig. 7(a) were collected and are presented in Fig. 7(b-d), where each region contains a weld. The weld interface in Fig. 7(b) within the amorphous region shows sparse spherulites in the bulk of the extruded layer. At the interface a higher spherulite fraction can be observed. Near an interface in the transition region the density and size of the spherulites increase (Fig. 7(c)), with an associated increase in the crystalline fraction at the weld line. In comparison to the amorphous region, the spherulites are more spherical and symmetric suggesting longer growth times. In the highly crystalline region, the weld interface is indistinguishable from the bulk crystallinity which is densely occupied with spherulites (Fig. 7(d)). The increase in interfacial crystallinity with bulk crystallinity is consistent with the idea that as more crystallites are allowed to form during printing, the fraction of the interface between printed layers that is able to weld is reduced, limiting weld strength.

As the chamber temperature increases from from 70 °C to 130 °C, it is anticipated that the cooling rate of the deposited PEEK decreases such that the printed extruded layer spends more time in the temperature range (approx. 180–240 °C) for PEEK cold crystallization where the crystallization half time, $\tau_{1/2}$ can be less than a second. [48–52] A simple finite element heat transfer model (see Fig. S2 in the Supporting Information) indicates that the change in chamber temperature from 70 °C to 130 °C can indeed cause a differentiation in the cooling rate within the cold crystallization regime, supporting the significant increase in crystallinity observed with an increase in chamber temperature from 70–130 °C. Avrami analysis of the isothermal cold crystallization in

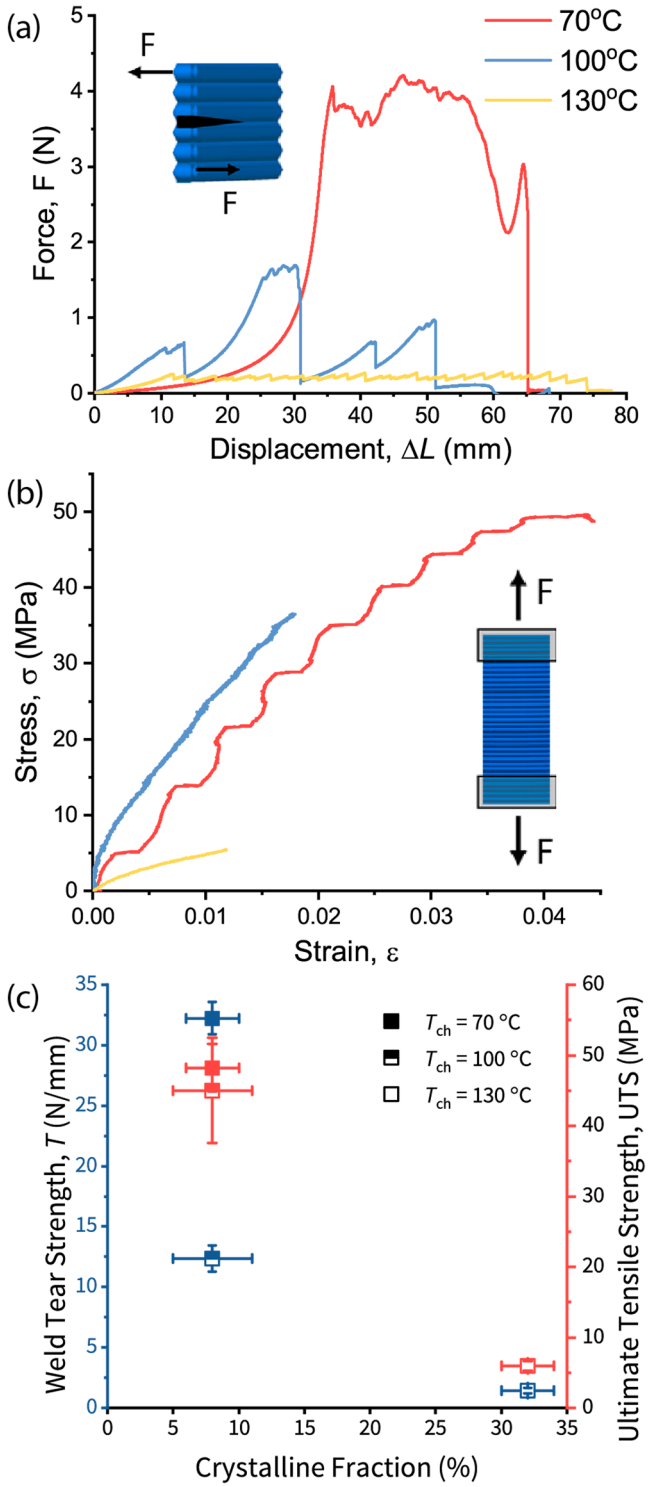

Fig. 4. (a) Representative plots of force as a function of grip displacement for Mode III tear testing of welds in FFF-PEEK. Inset: Loading configuration of weld in the tearing test. Each curve demonstrates typical behavior for samples printed at each of the three chamber temperatures. (b) Stress-strain curves of samples tested in tension for each of the three chamber temperatures. Inset: Loading configuration of weld in the tensile test. The oscillatory behavior observed for $T_{ch} = 70$ °C is the result of the printed layers interfering with the video extensometer measurement of strain. (c) Weld tearing strength (blue) and UTS (red) for each of the three chamber temperatures tested. Error bars represent one standard deviation. For tearing energy measurements, at least 5 samples were tested for each T_{ch}. For UTS measurements, 3 samples were tested for $T_{ch} = 70$ and 100 °C whereas 2 samples were tested for $T_{ch} = 130$ °C due to the fragility of the samples printed at $T_{ch} = 130$ °C.

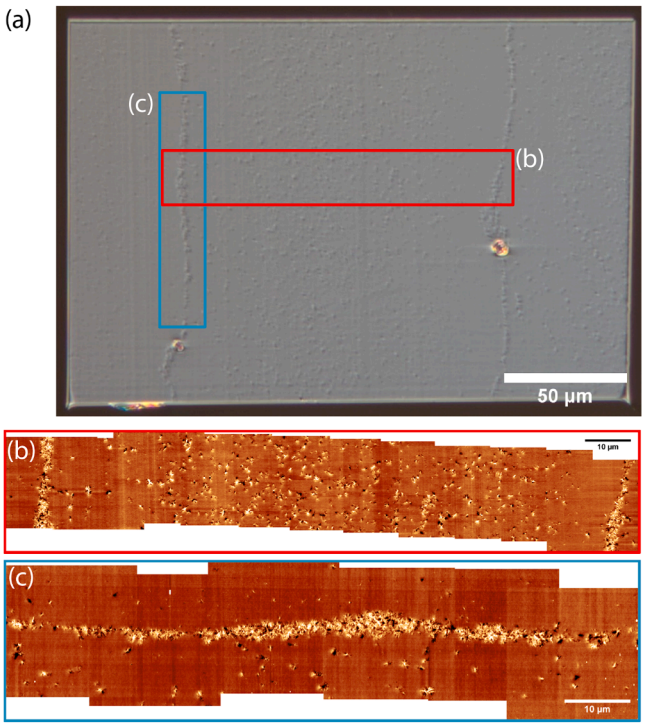

Fig. 5. (a) DIC optical image of ultra-microtomed surface for a single printed extruded layer and its welds with neighboring extruded layers. The areas imaged with AFM are indicated by the colored rectangles. Texture in the image is the result of exposed spherulites. (b) Stitched AFM height images across the central extruded layer from one weld interface to the other within the region indicated by the red rectangle in (a). (c) Stitched AFM height images of the weld interface within the blue rectangle indicated in (a). The AFM measurement parameters are $A_{0,3} = 3.2$ nm, $A_3 = 2.1$ nm, $f_{0,3} = 1221.7$ kHz, $Q_3 = 584.99$.

as-printed samples confirms that the crystallization kinetics is greatly accelerated approximately 20 °C above T_g (see section S3 in the Supporting Information) for the Ketaspire PEEK grade used here. Within the range of temperatures studied for crystallization kinetics, we find that the crystallization rate of the Ketaspire PEEK used is slower to crystallize than commonly used PEEK grades such as Victrex 450 G [5,7,50,53] but faster than a PEEK termed Victrex AM 200 recently developed specifically for fused filament fabrication and characterized by Yi *et. al.* [16] Further work in developing the heat transfer model to include non-linear behavior is underway to refine our understanding of the thermal history of PEEK and subsequent crystallization.

While the high number of crystalline domains at the weld interface is consistent with modelling of material extrusion that includes flow induced crystallization, [43] alternative mechanisms that could also explain the sudden increase in interface crystallinity are not ruled out by this work. For example, three alternative explanations are: 1) free surface mediated crystallinity in which the added mobility of polymer chains at the free surface allows for premature and rapid crystallization compared to the polymer bulk, [54,55] 2) different thermal history at the surface layer of an extruded layer as result of radiant heat transfer from the printer nozzle, or 3) heterogenous crystal growth at the weld interface due to trapped impurities or surface defects. Further work is needed to confirm what mechanism is responsible for the weld interface morphology observed here.

3.4. Annealing of amorphous as-printed specimens

The high weld strength that results from printing with $T_{ch} = 70$ °C presents a potential opportunity to produce strong, fully crystallized additively manufactured PEEK components by using a post-print anneal

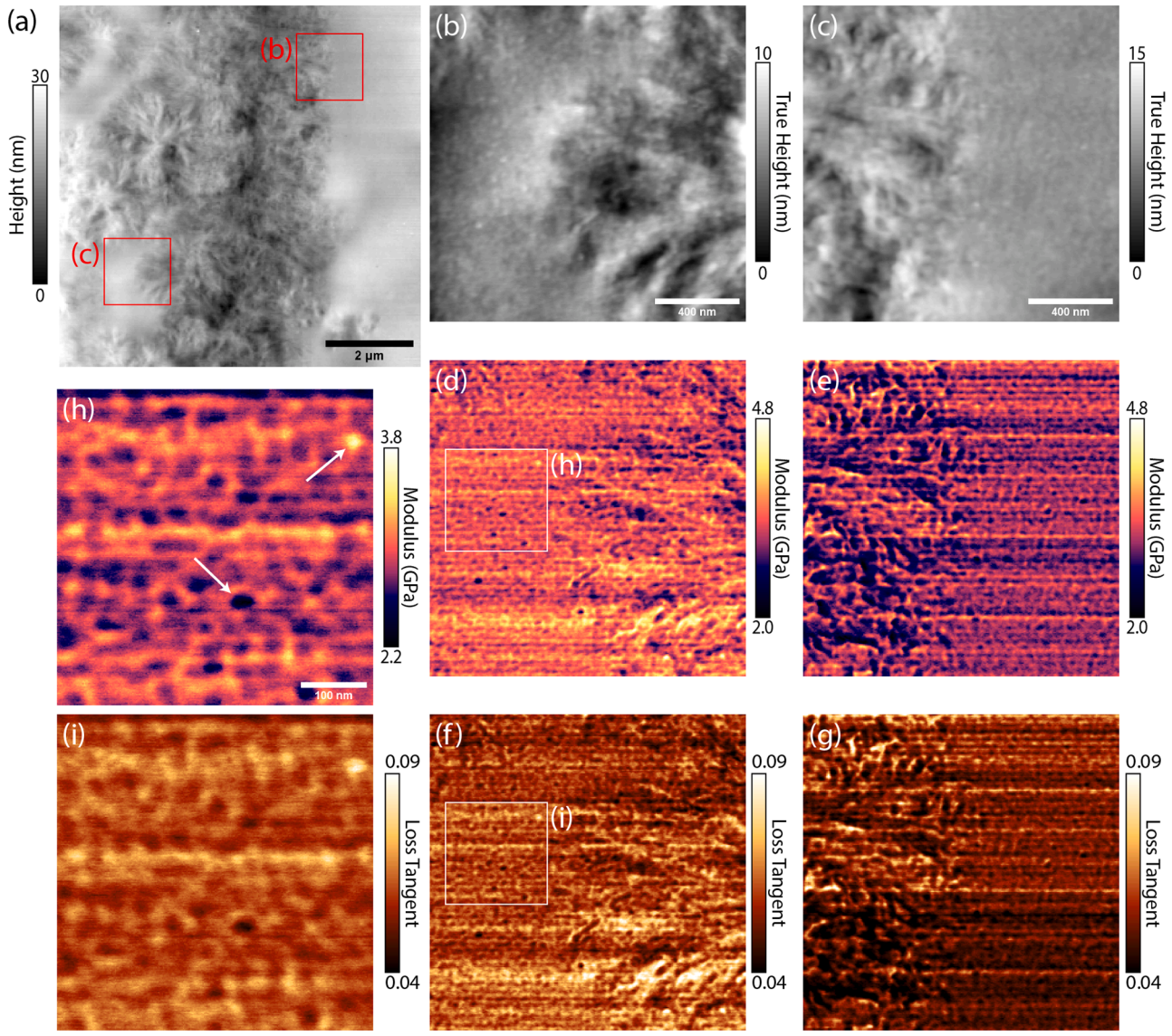

Fig. 6. AM-FM mechanical mapping of FFF-PEEK interfaces. (a) Height image of a fully crystalline interface between two printed extruded layers with regions for targeted analysis indicated with red squares. (b-c) Sample deformation corrected height maps of the regions indicated in (a). Corresponding maps of (d-e) Hertzian modulus and (f-g) loss tangent. (h-i) High resolution (h) modulus and (i) loss tangent maps of the region indicated by the white square in (d). Examples of nodules with anomalous mechanical properties are indicated in (h). The measurement parameters are $A_{0,1} = 115.6$ nm, $A_1 = 77.4$ nm, $f_{0,1} = 62.199$ kHz, $k_1 = 2.00$ N/m $Q_1 = 141.14$, $A_2 = 2.7$ nm, $f_{0,2} = 381.706$ kHz, $k_2 = 43.853$ N/m, $a = 2$ nm.

to cold crystallize the printed parts and induce co-crystallization across the weld. While the amorphous FFF-PEEK demonstrates good mechanical properties, the full mechanical strength and chemical inertness of bulk PEEK is realized when the polymer is fully crystallized. [41,56,57] As such, we examine whether a printing and post-processing procedure can enable FFF-PEEK to obtain properties comparable to bulk crystalline PEEK. The major barrier to strong, fully crystalline, FFF-PEEK parts, as laid out in Sections 3.2 and 3.3, is the premature crystallization causing a barrier to weld formation during printing, preventing effective chain entanglement [18,58] and co-crystallization[20] across the welds between extruded layers.

Co-crystallization requires that the polymer chains near the weld are returned to equilibrium conformations and allowed to entangle across the weld during annealing before crystallization occurs. Therefore, a two-step annealing process is investigated, where a low temperature annealing step above T_g, but below T_{cc} is first used to encourage chain diffusion and weld healing. The low temperature anneal is then followed by a high temperature annealing step above T_{cc} to induce cold crystallization. It is clear from Fig. 3 that a low temperature annealing step must occupy the very small temperature range between the T_g and T_{cc} of the printed PEEK. Exploratory annealing at a range of temperatures in the DSC (Fig. 8(a)) over 12 hrs demonstrates the thermally activated nature of cold crystallization, with crystallization observed above 150 °C (Fig. 8(b)), but no significant change below 148 °C. Therefore, an annealing temperature to relax the weld structure but prevent crystallization should be below 150 °C, but above the as-printed T_g of 143 °C so that the chains have some mobility. After the annealing step below 150 °C is conducted to promote weld formation at the molecular level, an additional crystallization step above 150 °C will be used to fully crystallize FFF-PEEK samples printed with $T_{ch} = 70$ °C. For the following two-step annealing studies an initial annealing temperature of 148 °C is maintained for 6 h for weld healing, followed by an anneal at 180 °C for another 6 hrs to induce crystallization. In addition, other samples are annealed at either 148 °C or 180 °C for 12 h for comparison to the two-step annealing procedure. The weld and tensile strength of the annealed samples is then compared to the as-printed samples.

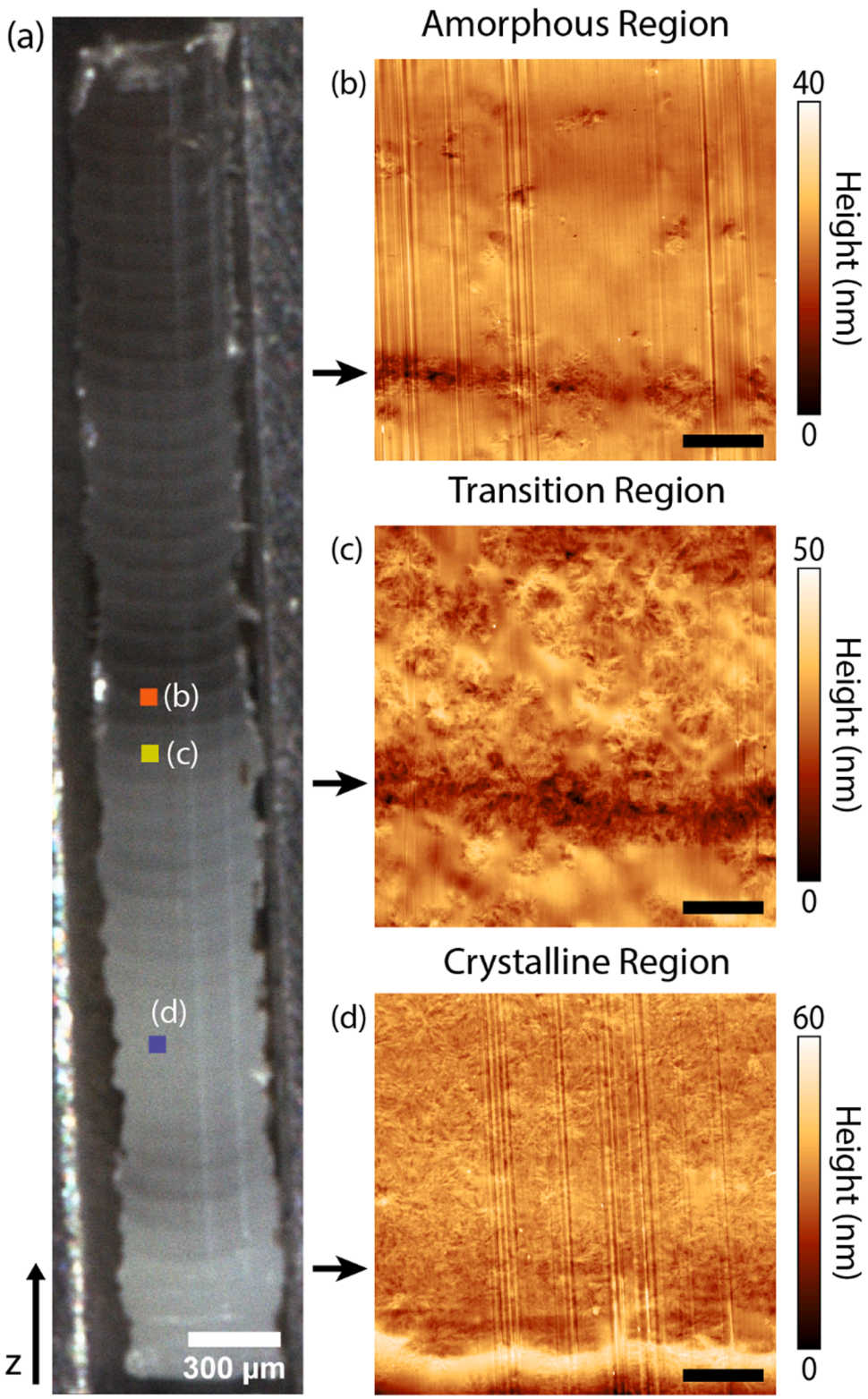

Fig. 7. (a) Large scale optical image of the microtomed cross-section of the FFF printed sample near the print bed. The printing direction from the build plate is indicated with the arrow labelled *z*. White, opaque regions indicate highly crystalline regions. Dark transparent regions indicate amorphous regions. The areas targeted for AFM imaging are indicated with colored squares. (b) Weld interface in the amorphous region of the sectioned surface. Isolated spherulites are observed in the bulk of the extruded layer along with interface crystallinity. (c) Weld interface in a transition region with moderate crystallinity. Higher spherulite density in the bulk is observed compared to the amorphous region, with a fully crystalline interface. (d) Weld interface in a highly crystalline region of the sectioned surface. Any crystallinity at the weld is nearly indistinguishable from the bulk crystallinity. Black scale bar in (b-d) indicates 4 μm. Black arrows in (b-d) indicate the location of the weld line between printed layers. The typical AFM measurement parameters are $A_{0,1} = 56.1$ nm, $A_1 = 37.0$ nm, $f_{0,1} = 62.205$ kHz, $Q_1 = 170.44$.

The tensile and tearing strength of the single-step and two-step annealed FFF-PEEK samples is provided in Fig. 9 along with the as-printed samples with $T_{ch} = 70$ °C and 130 °C. Representative tearing curves and tensile stress-strain curves for annealed samples are provided in Fig. S4 in the Supporting Information. For all annealing conditions, tensile specimens continued to exclusively fail at the weld interface between extruded layers.

The two-step annealed, crystalline PEEK demonstrates a significant 6–8 × improvement in tensile strength over the comparably crystalline samples printed at $T_{ch} = 130$ °C (Fig. 9(a)). Two-step annealed PEEK also shows modestly improved mechanical properties over the fully crystalline PEEK one-step annealed at 180 °C. The measured UTS of 37 MPa for the two-step annealed, crystalline sample remains much lower than the expected UTS of 95 MPa for bulk Ketaspire™ PEEK,

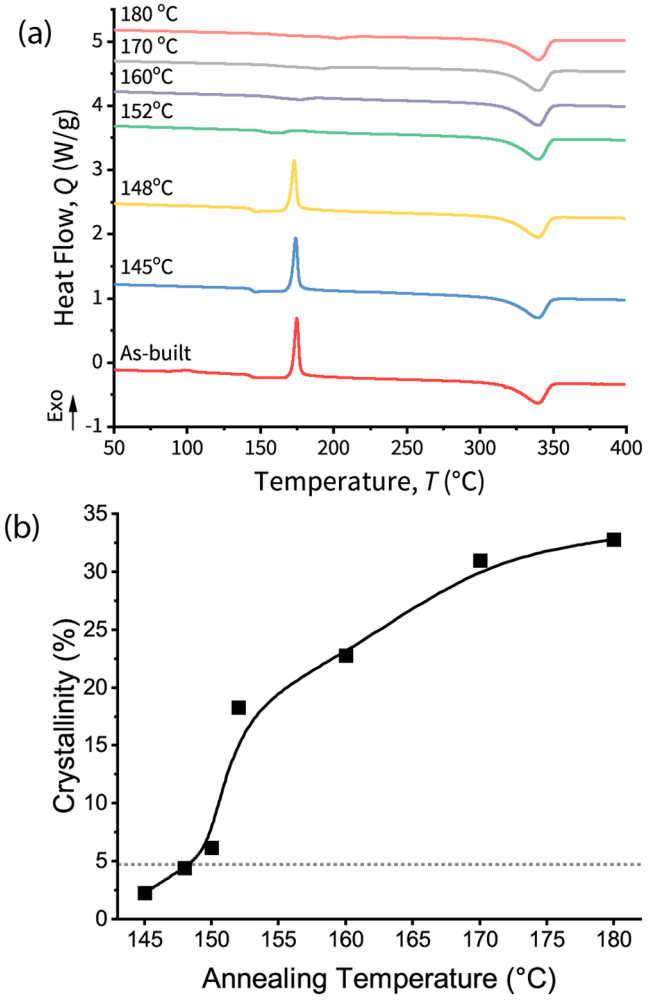

Fig. 8. (a) DSC traces of PEEK samples printed with $T_{ch} = 70$ °C upon heating at 10 °Cmin^{-1} after annealing at the indicated temperatures for 12 hrs. (b) Resulting crystalline percentage after annealing for 12 hrs. The dotted gray line indicates the measured crystallinity of the bulk polymer after printing at $T_{ch} = 70$ °C. The black line is a guide to the eye.

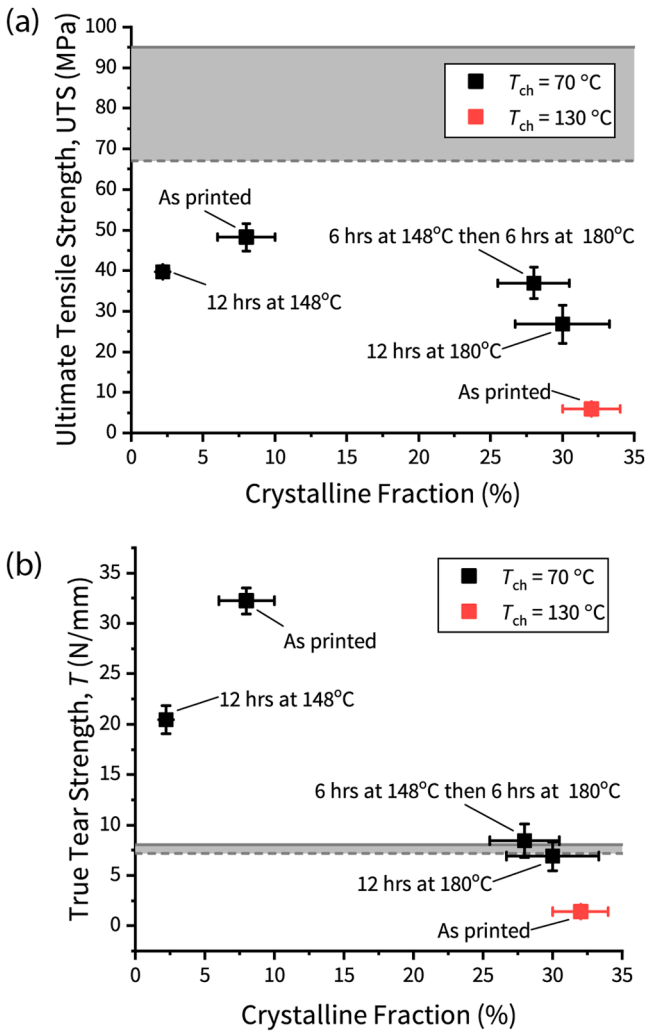

Fig. 9. Comparison of (a) ultimate tensile strength and (b) weld tearing strength as a function of bulk crystallinity for as printed and annealled samples. Each data point is labeled with the annealing conditions or 'as printed' for unannealed samples. The grey regions represent the range of (a) UTS and (b) tearing strength values observed for bulk PEEK with the upper bound (solid gray line) the strength for fully crystallized PEEK and the lower bound the strength of fully amorphous PEEK (dashed grey line). The nominal tensile strength for amorphous and crystalline PEEK is estimated from Chivers *et. al.* [41] and the data sheet for Ketaspire™ PEEK (Solvay, USA) respectively. The nominal tear strength for amorphous and crystalline PEEK is measured directly from provided Ketaspire™ PEEK films.

despite the tearing strength recovering to conincide with film tearing measurements (Fig. 9(b)). The decrease in tensile strength of FFF-PEEK compared to bulk PEEK is therefore likely, at least in part, due to the notch sensitivity of crystalline PEEK in tension which promotes brittle fracture at the neck that forms between two printed layers (see Fig. 2 (d)). [59,60] However, the dramatic increase in strength compared to the as-printed PEEK with $T_{ch} = 130$ °C highlights the ability of two-step annealing to dramatically improve weld strength compared to PEEK that is allowed to crystallize during printing. The tensile strength of amorphous FFF-PEEK printed with $T_{ch} = 70$ °C remains higher than the tensile strength of the other samples, possibly due to non-equilibrium conformations at the weld.

The ultimate goal for FFF-PEEK is to achieve the tensile strength and full thermomechanical performance promised by bulk crystalline PEEK. Therefore, to reach tensile strengths within the upper range observed for bulk PEEK, efforts must be made to improve the tensile strength of crystalline FFF-PEEK. The initial results shown in Fig. 9 suggests that it is in fact possible to significantly improve the tensile strength of FFF-PEEK with appropriate processing conditions and material composition. Further optimization of printing and two-step annealing parameters should further improve the strength of crystalline FFF-PEEK.

The major increase in strength demonstrated here with two-step annealing should greatly assist the application of fully crystalline FFF-PEEK in functional, load-bearing devices. The identification of a very small 'goldilocks' zone between T_g and ~150 °C that enables chain relaxation without crystallization in PEEK may explain why previous annealing studies have had limited success with improving the strength of PEEK through annealing. [10,20] The ultimate goal with two-step annealing will be to achieve fully crystalline FFF-PEEK that can match bulk PEEK strength, but would likely require modification of the part geometry and polymer composition to minimize porosity and avoid the notch sensitivity of crystalline PEEK.

Curiously, the tearing energy of the amorphous FFF-PEEK (Fig. 9(b)) is dramatically increased compared to the tearing energy of crystalline and amorphous extruded PEEK films, which are measured to be 8.0 ± 0.1 N/mm and 7.2 ± 0.1 N/mm respectively. Meanwhile, the tearing strength of the annealed crystalline FFF-PEEK is similar to the crystalline film tearing strength suggesting that the high tear strengths (over 25 N/mm) observed for the as-printed amorphous welds formed at $T_{ch} = 70$ °C are due to the print conditions and not just sample geometry

(Table 2). Therefore, the high tear strength must be an intrinsic material property that is gained as a result of the additive manufacturing procedure.

The enhancement in weld tearing strength is possibly due to the non-equilibrium conformations of polymer chains at the weld that could form under extremely fast cooling and/or extrusion. [30–32,61] In comparison to the sample printed at $T_{ch} = 70$ °C, the sample printed with $T_{ch} = 100$ °C has an apparently similar crystallinity, but exhibits dramatically worse tearing strength (Fig. 4(c)). In addition, while the samples printed at $T_{ch} = 100$ °C visually appear crystalline (Fig. 1(c)) the samples printed at $T_{ch} = 70$ °C show no visual indication of crystallinity (Fig. 1(b)), suggesting that the crystalline fraction of samples printed with $T_{ch} = 70$ °C as measured by DSC is an overestimate of the true crystallinity of the samples. The artificially high crystallinity measured by DSC could be explained by the contribution from relaxation of non-equilibrium chain conformations formed during extrusion [61,62] to the measured enthalpy change during heating. This idea is also supported by the extended annealing at 148 °C causing a reduction in the apparent crystallinity of samples printed with $T_{ch} = 70$ °C (Fig. 9), suggesting that the extended heat treatment above T_g but below T_{cc} has allowed relaxation of the as-printed structure. However, the drastic increase in tear strength is not reflected in the UTS (Fig. 9(a)) of the parts printed at $T_{ch} = 70$ °C, which remains lower than the yield strength of bulk amorphous PEEK ($\sigma_{UTS} \approx 67$ MPa). [41] The drastic improvement in tear strength in amorphous FFF-PEEK is difficult to explain, and further study is underway to confirm the observed strengthening and determine the underlying mechanism.

Similarly to the tensile strength data, FFF-PEEK crystallized through the one-step and two-step annealing (Fig. 9(b)) shows improved properties compared to the fully crystalline FFF-PEEK printed with $T_{ch} = 130$ °C. In fact, the printing annealing procedures used in this study are sufficient to enable the crystalline FFF-PEEK to have weld tearing strengths comparable to or exceeding measurements made on homogenous extruded films. The improvement in tear strength relative to bulk measurements occurs even though the tensile strength of the annealed, crystalline samples remains lower than what is expected for bulk PEEK. Overall, the results in Fig. 9 suggests that the changes in material strength at the welds are anisotropic and the performance of PEEK welds is dependent on the failure mode.

This study focused on chambertemperatures between 70 °C and 130 °C, comparable to other recent studies.[10,14,16,19,42,63,64] However, there are several newer commercial printers capable of chamber temperatures > 200 °C. [53] Our current work is unable to comment on the mechanical performance of PEEK welds printed at these elevated temperatures. Studies on the crystallization kinetics of PEEK suggests that the crystallization rate slows significantly near the melting temperature of PEEK. [16,50] Therefore, a high temperature regime may exist that allows for strong welds to form before interfacial crystallization can prevent chain diffusion across printed layers. We hope to investigate PEEK welds printed at high temperatures in a future study.

4. Conclusion

Poly(ether ketone) (PEEK) has long been an attractive material for fused filament fabrication (FFF) due to its exceptional thermomechanical properties and chemical inertness. However, PEEK components manufactured via fused filament fabrication have suffered from poor and anisotropic mechanical properties due to low weld strength. Here we demonstrate that surface crystallization is the cause of the poor weld strength of FFF-PEEK for our processing conditions.

From atomic force microscopy of the weld zone in FFF-PEEK we find an increased density of crystallites at the weld interface compared to the interior of the extruded layer. The surface crystallization results in a hard, immobile 'skin' of crystallites on the surface of the deposited PEEK extruded layers that forms before subsequent layers can effectively weld and degrades the strength of the weld interface. To limit surface crystallization, the chamber temperature during printing is decreased from 130 °C to 70 °C so that predominantly amorphous PEEK parts are printed. A subsequent, two-step annealing procedure of the amorphous printed parts is designed to enable strong, fully crystallized PEEK parts. The first step takes advantage of a narrow temperature range above the glass transition temperature, but below the cold crystallization temperature of PEEK to allow for weld healing without crystallization. The second annealing step is conducted above the cold crystallization temperature to yield FFF-PEEK that is ≈ 30% crystalline. We demonstrate that this carefully controlled printing and annealing can improve the ultimate tensile strength across the weld from 6 MPa to 37 MPa and produce weld tearing strengths comparable to bulk PEEK films for semi-crystalline FFF-PEEK parts. Further investigation is required to determine optimum annealing times for weld healing based on the polymer rheology and diffusion kinetics between T_g and T_{cc}. During this study, we also observed that printing amorphous PEEK parts results in a weld tearing strength of 32 N/mm, much higher than the 7 N/mm tearing strength measured on amorphous and crystalline extruded PEEK films. The cause of the observed enhancement in weld strength needs additional investigation.

CRediT authorship contribution statement

David W. Collinson: Conceptualization, Methodology, Validation, Formal analysis, Investigation, Writing – original draft, Visualization. **Natalia Von Windheim**: Conceptualization, Methodology, Validation, Formal analysis, Investigation, Visualization, Writing – review and editing. **Ken Gall:** Conceptualization, Resources, Supervision, Project administration, Funding acquisition, Writing – review and editing. **L. Catherine Brinson**: Conceptualization, Resources, Supervision, Project administration, Funding acquisition, Writing – review and editing.

Declaration of Competing Interest

The authors declare that they have no known competing financial interests or personal relationships that could have appeared to influence the work reported in this paper.

Acknowledgements

David W Collinson was supported by the National Science Foundation (NSF) (Award Number BCS-1734981, United States) L. Catherine Brinson was also supported by NSF (Award Number. CMMI-1818574, United States). Natalia von Windheim was supported by the Duke-Coulter Translational Partnership Grant (Award Number 291-0067, United States). This work was performed in part at the Duke University Shared Materials Instrumentation Facility (SMIF), a member of the North Carolina Research Triangle Nanotechnology Network (RTNN), which is supported by the National Science Foundation (award number ECCS-2025064, United States) as part of the National Nanotechnology Coordinated Infrastructure (NNCI). Thanks to Helmut Gnaegi at DiaTome for assistance with the wet sectioning procedure

Appendix A. Supporting information

Supplementary data associated with this article can be found in the online version at doi:10.1016/j.addma.2022.102604.

References

[1] D. Shukla, Y.S. Negi, J.S. Uppadhyaya, V. Kumar, Synthesis and modification of poly(ether ether ketone) and their properties: a review, Polym. Rev. 52 (2) (2012) 189–228.
[2] S. Singh, C. Prakash, S. Ramakrishna, 3D printing of polyether-ether-ketone for biomedical applications, Eur. Polym. J. 114 (2019) 234–248.

[3] T.D. Ngo, A. Kashani, G. Imbalzano, K.T.Q. Nguyen, D. Hui, Additive manufacturing (3D printing): a review of materials, methods, applications and challenges, Compos. Part B: Eng. 143 (2018) 172–196.

[4] P. Cebe, S.Y. Chung, S.-D. Hong, Effect of thermal history on mechanical properties of polyetheretherketone below the glass transition temperature, J. Appl. Polym. Sci. 33 (2) (1987) 487–503.

[5] M.F. Arif, S. Kumar, K.M. Varadarajan, W.J. Cantwell, Performance of biocompatible PEEK processed by fused deposition additive manufacturing, Mater. Des. 146 (2018) 249–259.

[6] D. Popescu, A. Zapciu, C. Amza, F. Baciu, R. Marinescu, FDM process parameters influence over the mechanical properties of polymer specimens: A review, Polym. Test. 69 (2018) 157–166.

[7] M. Rinaldi, T. Ghidini, F. Cecchini, A. Brandao, F. Nanni, Additive layer manufacturing of poly (ether ether ketone) via FDM, Compos. Part B: Eng. 145 (2018) 162–172.

[8] X. Gao, S. Qi, X. Kuang, Y. Su, J. Li, D. Wang, Fused filament fabrication of polymer materials: a review of interlayer bond, Addit. Manuf. 37 (2021), 101658.

[9] M. Fedel, V. Micheli, M. Thaler, F. Awaja, Effect of nitrogen plasma treatment on the crystallinity and self-bonding of polyetheretherketone (PEEK) for biomedical applications, Polym. Adv. Technol. 31 (2) (2020) 240–247.

[10] C. Basgul, T. Yu, D.W. MacDonald, R. Siskey, M. Marcolongo, S.M. Kurtz, Does annealing improve the interlayer adhesion and structural integrity of FFF 3D printed PEEK lumbar spinal cages? J. Mech. Behav. Biomed. Mater. 102 (2020), 103455.

[11] C. Yang, X. Tian, D. Li, Y. Cao, F. Zhao, C. Shi, Influence of thermal processing conditions in 3D printing on the crystallinity and mechanical properties of PEEK material, J. Mater. Process. Technol. 248 (2017) 1–7.

[12] C. Zawaski, C. Williams, Design of a low-cost, high-temperature inverted build environment to enable desktop-scale additive manufacturing of performance polymers, Addit. Manuf. 33 (2020), 101111.

[13] R. Wang, K.-j Cheng, R.C. Advincula, Q. Chen, On the thermal processing and mechanical properties of 3D-printed polyether ether ketone, MRS, Communications 9 (3) (2019) 1046–1052.

[14] B. Hu, X. Duan, Z. Xing, Z. Xu, C. Du, H. Zhou, R. Chen, B. Shan, Improved design of fused deposition modeling equipment for 3D printing of high-performance PEEK parts, Mech. Mater. 137 (2019), 103139.

[15] H.-D. Jung, T.-S. Jang, J.E. Lee, S.J. Park, Y. Son, S.-H. Park, Enhanced bioactivity of titanium-coated polyetheretherketone implants created by a high-temperature 3D printing process, Biofabrication 11 (4) (2019), 045014.

[16] N. Yi, R. Davies, A. Chaplin, P. McCutchion, O. Ghita, Slow and fast crystallising poly aryl ether ketones (PAEKs) in 3D printing: crystallisation kinetics, morphology, and mechanical properties, Addit. Manuf. 39 (2021), 101843.

[17] C.S. Davis, K.E. Hillgartner, S.H. Han, J.E. Seppala, Mechanical strength of welding zones produced by polymer extrusion additive manufacturing, Addit. Manuf. 16 (2017) 162–166.

[18] J.E. Seppala, S. Hoon Han, K.E. Hillgartner, C.S. Davis, K.B. Migler, Weld formation during material extrusion additive manufacturing, Soft Matter 13 (38) (2017) 6761–6769.

[19] C.-Y. Liaw, J.W. Tolbert, L.W. Chow, M. Guvendiren, Interlayer bonding strength of 3D printed PEEK specimens, Soft Matter 17 (18) (2021) 4775–4789.

[20] L. Martineau, F. Chabert, B. Boniface, G. Bernhart, Effect of interfacial crystalline growth on autohesion of PEEK, Int. J. Adhes. Adhes. 89 (2019) 82–87.

[21] Y.Q. Xue, T.A. Tervoort, P.J. Lemstra, Welding behavior of semicrystalline polymers. 1. The effect of nonequilibrium chain conformations on autoadhesion of UHMWPE, Macromolecules 31 (9) (1998) 3075–3080.

[22] Y.Q. Xue, T.A. Tervoort, S. Rastogi, J. Lemstra, Welding behavior of semicrystalline polymers. 2. Effect of cocrystallization on autoadhesion, Macromolecules 33 (19) (2000) 7084–7087.

[23] F. Awaja, Autohesion of polymers, Poly 97 (2016) 387–407.

[24] B.-R. Cho, J.L. Kardos, Consolidation and self-bonding in poly(ether ether ketone) (PEEK), J. Appl. Polym. Sci. 56 (11) (1995) 1435–1454.

[25] J.-F. Lamèthe, P. Beauchêne, L. Léger, Polymer dynamics applied to PEEK matrix composite welding, Aerosp. Sci. Technol. 9 (3) (2005) 233–240.

[26] N. von Windheim, D.W. Collinson, T. Lauc, L.C. Brinson, K. Gall, The influence of porosity, crystallinity, and interlayer adhesion on the tensile strength of 3D printed polylactic acid (PLA) Rapid Prototyp, J 27 (7) (2021) 1327–1336.

[27] W. Wang, J.M. Schultz, B.S. Hsiao, Anomalous two-stage spherulite growth in poly (aryl ether ketones) during isothermal crystallization, J. Polym. Sci., Part B: Polym. Phys. 34 (17) (1996) 3095–3105.

[28] Q. Sun, G.M. Rizvi, C.T. Bellehumeur, P. Gu, Effect of processing conditions on the bonding quality of FDM polymer filaments, Rapid Prototyp. J. 14 (2) (2008) 72–80.

[29] J. Bartolai, W. Simpson Timothy, R. Xie, Predicting strength of additively manufactured thermoplastic polymer parts produced using material extrusion, Rapid Prototyp. J. 24 (2) (2018) 321–332.

[30] J. Seo, A.M. Gohn, R.P. Schaake, D. Parisi, A.M. Rhoades, R.H. Colby, Shear flow-induced crystallization of Poly(ether ether ketone), Macromolecules 53 (9) (2020) 3472–3481.

[31] D. Parisi, J. Seo, B. Nazari, R.P. Schaake, A.M. Rhoades, R.H. Colby, Shear-induced isotropic–nematic transition in Poly(ether ether ketone) melts, ACS Macro Lett. 9 (7) (2020) 950–956.

[32] B. Nazari, A.M. Rhoades, R.P. Schaake, R.H. Colby, Flow-induced crystallization of PEEK: isothermal crystallization kinetics and lifetime of flow-induced precursors during isothermal annealing, ACS Macro Lett. 5 (7) (2016) 849–853.

[33] D.W. Collinson, P.V. Kolluru, N. Von Windheim, L.C. Brinson, Distribution of rubber particles in the weld zone of fused filament fabricated acrylonitrile butadiene styrene and the impact on weld strength, Addit. Manuf. 41 (2021), 101964.

[34] D.J. Blundell, B.N. Osborn, The morphology of poly(aryl-ether-ether-ketone), Poly 24 (8) (1983) 953–958.

[35] A. International, ASTM D1938–19, Standard Test Method for Tear-Propagation Resistance (Trouser Tear) of Plastic Film and Thin Sheeting by a Single-Tear Method, West Conshohocken, PA , 2019.

[36] D.W. Collinson, R.J. Sheridan, M.J. Palmeri, L.C. Brinson, Best practices and recommendations for accurate nanomechanical characterization of heterogeneous polymer systems with atomic force microscopy, Prog. Polym. Sci. 119 (2021), 101420.

[37] A. Labuda, M. Kocun, W. Meinhold, D. Walters, R. Proksch, Generalized Hertz model for bimodal nanomechanical mapping, Beilstein J. Nanotechnol. 7 (2016) 970–982.

[38] R. Proksch, M. Kocun, D. Hurley, M. Viani, A. Labuda, W. Meinhold, J. Bemis, Practical loss tangent imaging with amplitude-modulated atomic force microscopy, J. Appl. Phys. 119 (13) (2016), 134901, 134901/1-11.

[39] R. Proksch, D.G. Yablon, Loss tangent imaging: theory and simulations of repulsive-mode tapping atomic force microscopy, Appl. Phys. Lett. 100 (7) (2012), 073106/1-3.

[40] S. Benaglia, C.A. Amo, R. Garcia, Fast, quantitative and high resolution mapping of viscoelastic properties with bimodal AFM, Nanoscale 11 (32) (2019) 15289–15297.

[41] R.A. Chivers, D.R. Moore, The effect of molecular weight and crystallinity on the mechanical properties of injection moulded poly(aryl-ether-ether-ketone) resin, Poly 35 (1) (1994) 110–116.

[42] J. Pu, C. McIlroy, A. Jones, I. Ashcroft, Understanding mechanical properties in fused filament fabrication of polyether ether ketone, Addit. Manuf. (2020), 101673.

[43] C. McIlroy, R.S. Graham, Modelling flow-enhanced crystallisation during fused filament fabrication of semi-crystalline polymer melts, Addit. Manuf. 24 (2018) 323–340.

[44] T.H. Sauer, J.H. Wendorff, H.J. Zimmermann, Thermotropic rigid-chain copolymers: X-ray investigations of the structure, J. Polym. Sci., Part B: Polym. Phys. 25 (12) (1987) 2471–2485.

[45] F.O. Oladoyinbo, D.F. Lewis, D.J. Blundell, H.M. Colquhoun, A thermotropic poly (ether ketone) based on the p-quaterphenyl unit: evidence for a smectic C phase, Polym. Chem. 11 (1) (2020) 75–83.

[46] M. Ballauff, Stiff-chain polymers—structure, phase behavior, and properties, Angew. Chem. Int. Ed. Engl. 28 (3) (1989) 253–267.

[47] I. Coccorullo, R. Pantani, G. Titomanlio, Spherulitic nucleation and growth rates in an iPP under continuous shear flow, Macromolecules 41 (23) (2008) 9214–9223.

[48] A.M. Gohn, J. Seo, R.H. Colby, R.P. Schaake, R. Androsch, A.M. Rhoades, Crystal nucleation in poly(ether ether ketone)/carbon nanotube nanocomposites at high and low supercooling of the melt, Poly 199 (2020), 122548.

[49] W. Wang, J.M. Schultz, B.S. Hsiao, Dynamic study of crystallization- and melting-induced phase separation in PEEK/PEKK blends, Macromolecules 30 (16) (1997) 4544–4550.

[50] J. Seo, A.M. Gohn, O. Dubin, H. Takahashi, H. Hasegawa, R. Sato, A.M. Rhoades, R. P. Schaake, R.H. Colby, Isothermal crystallization of poly(ether ether ketone) with different molecular weights over a wide temperature range, Polym. CRYSTALLIZATION 2 (1) (2019), e10055.

[51] C. Fougnies, M. Dosière, M.H.J. Koch, J. Roovers, Cold crystallization of narrow molecular weight fractions of PEEK, Macromolecules 32 (24) (1999) 8133–8138.

[52] T. Liu, Z. Mo, S. Wang, H. Zhang, Nonisothermal melt and cold crystallization kinetics of poly(aryl ether ether ketone ketone), Polym. Eng. Sci. 37 (3) (1997) 568–575.

[53] A. Das, C.A. Chatham, J.J. Fallon, C.E. Zawaski, E.L. Gilmer, C.B. Williams, M. J. Bortner, Current understanding and challenges in high temperature additive manufacturing of engineering thermoplastic polymers, Addit. Manuf. 34 (2020), 101218.

[54] S. Luo, X. Kui, E. Xing, X. Wang, G. Xue, C. Schick, W. Hu, E. Zhuravlev, D. Zhou, Interplay between free surface and solid interface nucleation on two-step crystallization of Poly(ethylene terephthalate) thin films studied by fast scanning calorimetry, Macromolecules 51 (14) (2018) 5209–5218.

[55] K. Taguchi, H. Miyaji, K. Izumi, A. Hoshino, Y. Miyamoto, R. Kokawa, Crystal growth of isotactic polystyrene in ultrathin films: film thickness dependence, J. Macromol. Sci., Part B 41 (4–6) (2002) 1033–1042.

[56] I.V. Panayotov, V. Orti, F. Cuisinier, J. Yachouh, Polyetheretherketone (PEEK) for medical applications, JMSMM 27 (7) (2016) 118.

[57] S.M. Kurtz, J.N. Devine, PEEK biomaterials in trauma, orthopedic, and spinal implants, Biomaterials 28 (32) (2007) 4845–4869.

[58] Y.S. Ko, D. Herrmann, O. Tolar, W.J. Elspass, C. Brändli, Improving the filament weld-strength of fused filament fabrication products through improved interdiffusion, Addit. Manuf. 29 (2019), 100815.

[59] M.C. Sobieraj, S.M. Kurtz, C.M. Rimnac, Notch sensitivity of PEEK in monotonic tension, Biomaterials 30 (33) (2009) 6485–6494.

[60] K.M. Conway, G.J. Pataky, Crazing in additively manufactured acrylonitrile butadiene styrene, EnFM 211 (2019) 114–124.

[61] C. McIlroy, P.D. Olmsted, Disentanglement effects on welding behaviour of polymer melts during the fused-filament-fabrication method for additive manufacturing, Poly 123 (2017) 376–391.

[62] C. McIlroy, P.D. Olmsted, Deformation of an amorphous polymer during the fused-filament-fabrication method for additive manufacturing, J. Rheol. 61 (2) (2017) 379–397.
[63] M. Garcia-Leiner, B. Streifel, C. Başgül, D.W. MacDonald, S.M. Kurtz, Characterization of polyaryletherketone (PAEK) filaments and printed parts produced by extrusion-based additive manufacturing, Polym. Int. 70 (8) (2021) 1128–1136.
[64] M. Vaezi, S. Yang, Extrusion-based additive manufacturing of PEEK for biomedical applications, Virtual Phys. Prototyp. 10 (3) (2015) 123–135.